REVISITING IMPACTS OF NUCLEAR BURNING FOR REVIVING WEAK SHOCKS IN NEUTRINO-DRIVEN SUPERNOVAE

KO NAKAMURA[1,2], TOMOYA TAKIWAKI[3], KEI KOTAKE[1,4], AND NOBUYA NISHIMURA[5,6]
[1] Division of Theoretical Astronomy, National Astronomical Observatory of Japan, 2-21-1 Osawa, Mitaka, Tokyo, 181-8588, Japan
[2] Faculty of Science and Engineering, Waseda University, Phkubo 3-4-1, Shinjuku, Tokyo, 169-8555, Japan
[3] Center for Computational Astrophysics, National Astronomical Observatory of Japan, 2-21-1 Osawa, Mitaka, Tokyo, 181-8588, Japan
[4] Department of Applied Science, Fukuoka University, 8-19-1, Nanakuma, Jonan-ku, Fukuoka, 814-0180, Japan
[5] Astrophysics Group, iEPSAM, Keele University, Keele, ST5 5BG, UK
[6] Department of Physics, University of Basel, Klingelbergstrasse 82, 4056 Basel, Switzerland

ABSTRACT

We revisit potential impacts of nuclear burning on the onset of the neutrino-driven explosions of core-collapse supernovae. By changing the neutrino luminosity and its decay time to obtain parametric explosions in one- and two-dimensional (1D and 2D, respectively) models with or without a 13 isotope α network, we study how the inclusion of nuclear burning could affect the postbounce dynamics for 4 progenitor models; 3 for 15.0 $M_\odot$ stars and 1 for an 11.2 $M_\odot$ star. We find that the energy supply due to the nuclear burning of infalling material behind the shock can energize the shock expansion, especially for models that produce only marginal explosions in the absence of nuclear burning. These models are energized by nuclear energy deposition when the shock front passes through the silicon-rich layer and/or later as it touches the oxygen-rich layer. Depending on the neutrino luminosity and its decay time, the diagnostic energy of the explosion increases up to a few times 10^{50} erg for models with nuclear burning compared to the corresponding models without. We point out that these features are most remarkable for the Limongi–Chieffi progenitor in both 1D and 2D because the progenitor model possesses a massive oxygen layer, with an inner-edge radius that is smallest among the employed progenitors, which means that the shock can touch the rich fuel on a shorter timescale after bounce. The energy difference is generally smaller ($\sim$0.1–0.2 $\times 10^{51}$ erg) in 2D than in 1D (at most $\sim$0.6 $\times 10^{51}$ erg). This is because neutrino-driven convection and the shock instability in 2D models enhance the neutrino heating efficiency, which makes the contribution of nuclear burning relatively smaller compared to 1D models. Considering uncertainties in progenitor models, our results indicate that nuclear burning should remain one of the important ingredients to foster the onset of neutrino-driven explosions.

Key words: hydrodynamics – neutrinos – nuclear reactions, nucleosynthesis, abundances – supernovae: general

Online-only material: color figures

1. INTRODUCTION

For more than four decades, since the dawn of modern core-collapse supernova (CCSN) theory, the neutrino-heating mechanism (Colgate & White 1966), in which a supernova (SN) shock is revived by neutrino energy deposition to trigger explosions (Wilson 1985; Bethe & Wilson 1985), has been the leading candidate for the explosion mechanism. However, the simplest, spherically symmetric (1D) form of this mechanism fails, except for super-asymptotic-giant-branch stars at the low-mass end (Müller et al. 2012a), to explode canonical massive stars (Rampp & Janka 2000; Liebendörfer et al. 2001; Thompson et al. 2003; Sumiyoshi et al. 2005). Pushed by accumulating SN observations of the blast morphology (e.g., Wang & Wheeler 2008; Tanaka et al. 2012 and references therein), a number of multi-dimensional (multi-D) hydrodynamic simulations have been reported, which gives us confidence that hydrodynamic motions associated with convection (e.g., Herant et al. 1992; Burrows et al. 1995; Janka & Müller 1996; Fryer et al. 2002; Fryer 2004) and the Standing-Accretion-Shock-Instability (SASI; e.g., Blondin et al. 2003; Scheck et al. 2004, 2006; Ohnishi et al. 2006, 2007; Ott et al. 2008; Murphy & Burrows 2008; Foglizzo et al. 2006, 2007, 2012; Endeve et al. 2012; Iwakami et al. 2008, 2009; Fernández & Thompson 2009a, 2009b; Fernández 2010; Hanke et al. 2012; Fernández

et al. 2013) can help the onset of neutrino-driven explosions (see collective references in Janka 2012; Kotake et al. 2012c).

In fact, neutrino-driven explosions have been obtained in first-principle two- and three-dimensional (2D and 3D, respectively) simulations in which spectral neutrino transport is solved by various approximations (e.g., Kotake et al. 2012). The Garching group (Buras et al. 2006a, 2006b; Marek & Janka 2009; Hanke et al. 2013; Müller et al. 2011, 2012a, 2012b, 2013) included one of the best available neutrino transfer approximations by the ray-by-ray variable Eddington factor method. The Oak Ridge group (Bruenn et al. 2009, 2013) included a ray-by-ray multi-group flux-limited diffusion transport with the best available weak interactions. The Nippon group[7] (Suwa et al. 2010, 2011, 2013; Takiwaki et al. 2012, 2013) employed a ray-by-ray isotropic diffusion source approximation (Liebendörfer et al. 2009) with a reduced set of weak interactions.[8]

This success, however, brings to light new questions. The explosion energies obtained in some 2D models are smaller by up to a factor of 10 compared to the canonical SN kinetic energy ($\sim$$10^{51}$ erg; see Table 1 in Kotake 2013 for a current summary). So what is missing? One study has shown that

---

[7] We call our team "Nippon" because it is the Japanese translation of "Japan."
[8] See Sumiyoshi & Yamada (2012) for collective references about detailed neutrino transport schemes.

3D hydrodynamics can boost the onset of neutrino-driven explosions compared to 2D (Nordhaus et al. 2010), although this is still under considerable debate (Hanke et al. 2012, 2013; Takiwaki et al. 2012; Couch 2013b). Recently, general relativity was reported to help the onset of multi-D neutrino-driven explosions by Müller et al. (2011, 2012b) in 2D simulations with detailed neutrino transport and by Kuroda et al. (2012, 2013) in 3D simulations, but with approximate neutrino transport. The impacts of nuclear equations of state (EOSs) have been investigated in multi-D simulations by Marek & Janka (2009), Marek et al. (2009), Suwa et al. (2013), and Couch (2013a). However, there is still room to study more detailed nuclear physical impacts in these first principle multi-D simulations, such as the density dependence of symmetry energy and the skewness of compressibility (Steiner et al. 2010; Lattimer & Lim 2013) and influences of light nuclei (e.g., Sumiyoshi & Röpke 2008; Arcones et al. 2008; Nakamura et al. 2009) and of inelastic neutrino-nucleus scattering (e.g., Haxton 1988; Ohnishi et al. 2007; Langanke et al. 2008) on enhancing the neutrino heating rates in the gain region. More recently, impacts of improved neutrino interactions based on the 1D full Boltzmann simulations have been elaborately investigated (Lentz et al. 2012a, 2012b). The neutrino-driven mechanism would be assisted by other candidate mechanisms, such as the acoustic mechanism (e.g., Burrows et al. 2006) or the magnetohydrodynamic mechanism (e.g., Kotake et al. 2004a, 2004b; Takiwaki et al. 2004, 2009; Burrows et al. 2007; Guilet et al. 2011; Obergaulinger & Janka 2011; Takiwaki & Kotake 2011; see also Kotake et al. 2006 for collective references therein). Other possibilities include quark-hadron phase transitions in the core of the protoneutron star (e.g., Takahara & Sato 1988; Sagert et al. 2009), viscous heating by the magnetorotational instability (Thompson et al. 2005), or energy dissipation via Alfvén waves (Suzuki et al. 2008).

Joining in these efforts to look for some possible ingredients to foster explosions, we studied the roles of nuclear burning. To the best of our knowledge, Janka et al. (2001) were the first to clearly point out that an additional energy released by the nuclear burning of infalling material behind the shock could make a significant contribution to the explosion energy (see their Equation (5)). The mass in the silicon (Si) layer, depending sensitively on the progenitor masses and structures, is in the range of $\sim$0.3–0.6 $M_\odot$ (Woosley & Weaver 1995; Woosley et al. 2002; Limongi & Chieffi 2006). Because the release of nuclear energy in Si burning is $\approx 10^{18}$ erg g^{-1}, a few 10^{50} erg are expected to be deposited by the explosive nuclear burning. It should be noted that nuclear burning has been included in the full-scale simulations by the Garching group (Rampp & Janka 2002; Buras et al. 2006a, 2006b; Marek & Janka 2009), in which composition changes of silicon, oxygen, (similarly neon and magnesium), and carbon, and their nuclear energy release are computed by a "flashing" treatment (see Appendix A, as well as Appendix B.2 in Rampp & Janka 2002). In a series of multi-D simulations in which neutrino transport is treated by a more approximate way to follow a long-term postbounce evolution in the context of the neutrino-driven mechanism, nuclear burning is included by a small network calculation (e.g., Kifonidis et al. 2003; Scheck et al. 2006; Wongwathanarat et al. 2010; Hammer et al. 2010; Arcones & Janka 2011; Ugliano et al. 2012). However, the impacts of nuclear burning on the SN dynamics have not been unambiguously investigated. In conference proceedings, the Oak Ridge group reported 2D explosion models based on their radiation-hydrodynamic

simulations (Bruenn et al. 2006; Mezzacappa et al. 2007) for 11.2 $M_\odot$ and 15.0 $M_\odot$ stars when an alpha network calculation was included, but not when they applied the flashing treatment. The authors pointed out that oxygen burning assists the (weak) shock to move farther out due to the additional pressure support in the vicinity of the weak shock. These situations motivate us to revisit the impacts of nuclear burning on assisting the shock propagation by performing hydrodynamic simulations, including a network calculation.

In the present work, we took the following strategy to see the roles of nuclear burning. First, in the spirit of Burrows & Goshy (1993) and Janka (2001), we attempted to find a critical condition in 1D, in which nuclear burning affects the criteria of explosion. Instead of performing full-scale radiation-hydrodynamic simulations, which are computationally expensive, we employ a light-bulb (LB) scheme to trigger explosions (e.g., Janka & Müller 1996) for the sake of our systematic survey. Previously, the role of nuclear burning has been shown to be negligible when using a very limited set of progenitor models, but we will show that, for a previously untested progenitor model, nuclear burning can push the weak shock farther out to help explosions.

Section 2 describes the numerical setup, including information about our hydrodynamic code with nuclear network and our initial models. Results are given in Section 3. After giving a detailed explanation about how nuclear burning 1D models could affect the postbounce dynamics (Sections 3.1 and 3.2), we move on to discuss our 2D models to study how nuclear burning interacts with multi-D hydrodynamics (Section 3.3). We summarize our results and discuss their implications in Section 4.

2. NUMERICAL SETUP

2.1. Hydrodynamics with Nuclear Network

We solve the hydrodynamic equations corresponding to the conservation of mass, momentum, and energy,

$$\frac{d\rho}{dt} + \rho \nabla \cdot \mathbf{v} = 0, \tag{1}$$

$$\rho \frac{d\mathbf{v}}{dt} = -\nabla p - \rho \nabla \Phi, \tag{2}$$

$$\frac{\partial e}{\partial t} + \nabla \cdot [(e + p)\mathbf{v}] = -p\mathbf{v} \cdot \nabla \Phi + \rho(H - C + Q), \tag{3}$$

where ρ is the mass density, $\mathbf{v}$ the fluid velocity, p the pressure, Φ the gravitational potential, and e the total energy density, respectively. The Lagrangian derivative is denoted by $d/dt \equiv \partial/\partial t + \mathbf{v} \cdot \nabla$. To treat Newtonian self-gravity, a monopole approximation is employed. The tabulated realistic EOS, based on the relativistic mean field theory (Shen et al. 1998), is implemented according to the prescription in Kotake et al. (2003). The term Q in Equation (3) denotes the net energy deposition rate by nuclear burning. The goal of this paper is to explore the effect of this term on shock revival. We compare two cases. (1) For the *burning* case, we estimate Q by calculating a simple nuclear reaction network, and (2) for the *non-burning* case, we do not solve the nuclear network ($Q = 0$), but adopt Shen EOS throughout our simulations.

For the *burning* case, we are keeping track of 13 species of α network (from ^{4}He to ^{56}Ni) by solving a separate advection equation for each species. The nuclear reaction network is mainly based on the REACLIB database (Rauscher &

Thielemann 2000). Experimentally determined masses (Audi & Wapstra 1995) and reactions (Angulo et al. 1999) are adopted if available. It should be noted that our network does not include the photodissociation of iron elements because Shen EOS adopted in this study takes these endothermic effects into account. It should also be noted that we solve the reaction network only for the grids where $T < 5 \times 10^9$ K, assuming that the local chemical composition is in nuclear statistical equilibrium above this temperature.

We also employ the LB scheme (Janka & Müller 1996), in which neutrino heating and cooling is adjusted parametrically to trigger explosions. Following Janka (2001) and Nordhaus et al. (2010), the neutrino heating (H) and cooling rates (C) in Equation (3) are given by,

$$H = 1.544 \times 10^{20} \left(\frac{L_{\nu_e}}{10^{52} \, \text{erg s}^{-1}} \right) \left(\frac{T_{\nu_e}}{4 \, \text{MeV}} \right)^2$$
$$\times \left(\frac{r}{100 \, \text{km}} \right)^{-2} (Y_n + Y_p) \, e^{-\tau_{\nu_e}} \, (\text{erg g}^{-1} \, \text{s}^{-1}), \tag{4}$$

$$C = 1.399 \times 10^{20} \left(\frac{T}{2 \, \text{MeV}} \right)^6 (Y_n + Y_p) \, e^{-\tau_{\nu_e}} \, (\text{erg g}^{-1} \, \text{s}^{-1}), \tag{5}$$

where L_{ν_e} is the electron-neutrino luminosity that is assumed to be equal to the anti-electron neutrino luminosity ($L_{\bar{\nu}_e} = L_{\nu_e}$), T_{ν_e} is the electron neutrino temperature assumed constant at 4 MeV, r is the distance from the center, T is the local fluid temperature, Y_n and Y_p are the neutron and proton fractions, respectively, and τ_{ν_e} is the electron neutrino optical depth, which we estimate according to Equation (7) in Hanke et al. (2012).

In this study, neutrino luminosity is assumed to evolve exponentially with time (Kifonidis et al. 2003) as

$$L_{\nu_e} = L_{\bar{\nu}_e} = L_{\nu 0} \exp(-t_{\text{pb}}/t_d), \tag{6}$$

where $L_{\nu 0}$ denotes the initial luminosity, t_{pb} is the time measured after core bounce, and t_d is the decay time, and $L_{\nu 0}$ and t_d are treated as free parameters. Neutrino heating and cooling are switched on only after core bounce, according to the prescriptions (Equations (4) and (5)) assuming $L_{\nu_e} = L_{\bar{\nu}_e}$ and $T_{\nu_e} = T_{\bar{\nu}_e}$. Before bounce, we employ the Y_e prescription proposed by Liebendörfer (2005), in which Y_e is given simply as a function of density, and after that, we refrain from solving the change of Y_e, following Murphy & Burrows (2008), Nordhaus et al. (2010) and Hanke et al. (2012; see, however, Ohnishi et al. 2006). As for the hydro-solver, we employ the ZEUS-MP code (Hayes et al. 2006), which has been modified for core-collapse simulations (e.g., Iwakami et al. 2008, 2009). The computational grid is comprised of 300 logarithmically spaced, radial zones from the center up to 5000 km. For 2D models we adopt coarse mesh points ($n_\theta = 32$ uniform grids) in the polar direction to make it possible to perform 174 models in 2D covering a wide range of the parameter region. For some selected models a finer resolution ($n_\theta = 128$) is taken.

In order to induce non-spherical instability after the stall of the prompt bounce shock, we added a radial velocity perturbation, $\delta v_r(r, \theta, \phi)$, to the steady spherically symmetric flow, according to the following equation,

$$v_r(r, \theta, \phi) = v_r^0(r) + \delta v_r(\theta, \phi), \tag{7}$$

with

$$\delta v_r = 0.01 \times \text{rnum} \times v_r^0(r, \theta), \tag{8}$$

Table 1
Summary of Progenitor Models and their Composition Features

Model	M_{total} ($M_\odot$)	M_{Fe} ($M_\odot$)	$R_{\text{Fe/Si}}$ (10^3 km)	M_{Si} ($M_\odot$)	$R_{\text{Si/O}}$ (10^3 km)	M_{O} ($M_\odot$)
LC15	13.4	1.44	1.31	0.221	2.22	0.814
WHW15	12.6	1.55	1.96	0.124	2.97	0.943
WW15	15.0	1.42	1.31	0.436	7.44	0.649
WHW11	10.8	1.24	1.00	0.168	3.74	0.289

Note. See the text for the definition of each quantity.

where $v_r^0(r, \theta)$ is the unperturbed radial velocity and δv_r is the random multi-mode perturbation with a random number $-1 < \text{rnum} < 1$.

2.2. Progenitor Models

In this study, we employ four progenitor models: three for 15.0 $M_\odot$ stars of Limongi & Chieffi (2006, hereafter LC15), Woosley & Weaver (1995, hereafter WW15), and Woosley et al. (2002, hereafter WHW15) and one for an 11.2 $M_\odot$ star of Woosley et al. (2002, hereafter WHW11). For all the models, Figure 1 shows the pre-collapse composition profiles from near the outer edge of the iron core to the outside. As we will explain in the next section, burning the oxygen shell behind the (weakly propagating) shock plays an important role in assisting the shock expansion. Therefore, the earlier the oxygen layer touches the (stalling) shock after bounce, the better it could work. Among the three variants of the 15 $M_\odot$ progenitors, the inner edge of the oxygen layer (seen as a sharp decline in solid red lines of Figure 1) is positioned much closer to the center for models LC15 (closest, top left panel) and WHW15 (next closest, top right panel) compared to model WW15 (bottom left panel). Table 1 shows a summary of the precollapse abundance distributions, in which each quantity, from the left to right column, corresponds to the different progenitor models, the progenitor mass, the mass of the iron core, the outer edge of the iron core, the mass of the silicon layer, the outer edge of the silicon layer, and the mass of the oxygen layer, respectively. The edge between each layer is defined as the radius where the most abundant element shifts from one to another (see Figure 1). The mass of oxygen layer for the 15 $M_\odot$ models of LC15 and WHW15 (M_O in the table) is larger than the other progenitors (i.e., WW15 and WHW11) and their oxygen layers (denoted by $R_{\text{Si/O}}$) are positioned much closer to the center, so that they can touch the SN shock in a shorter timescale after bounce (before the neutrino luminosity gets smaller with time). As one would anticipate, the impacts of nuclear burning are most remarkable for the LC15 progenitor as we will show in the later sections.

3. RESULTS

In Section 3.1, we start to investigate how the energy feedback from nuclear burning could affect the postbounce dynamics in 1D simulations. Then, in Section 3.2, we study how the nuclear-burning impacts are sensitive to the progenitor models, namely by the pre-collapse structures and their composition profiles. In Section 3.3, we then move on to discuss how nuclear burning would affect the 2D dynamics.

3.1. Impact of Nuclear Burning in 1D Simulations

Relying on the LB scheme in this study, the destiny of the stalling bounce shock (i.e., whether or not it will revive) depends
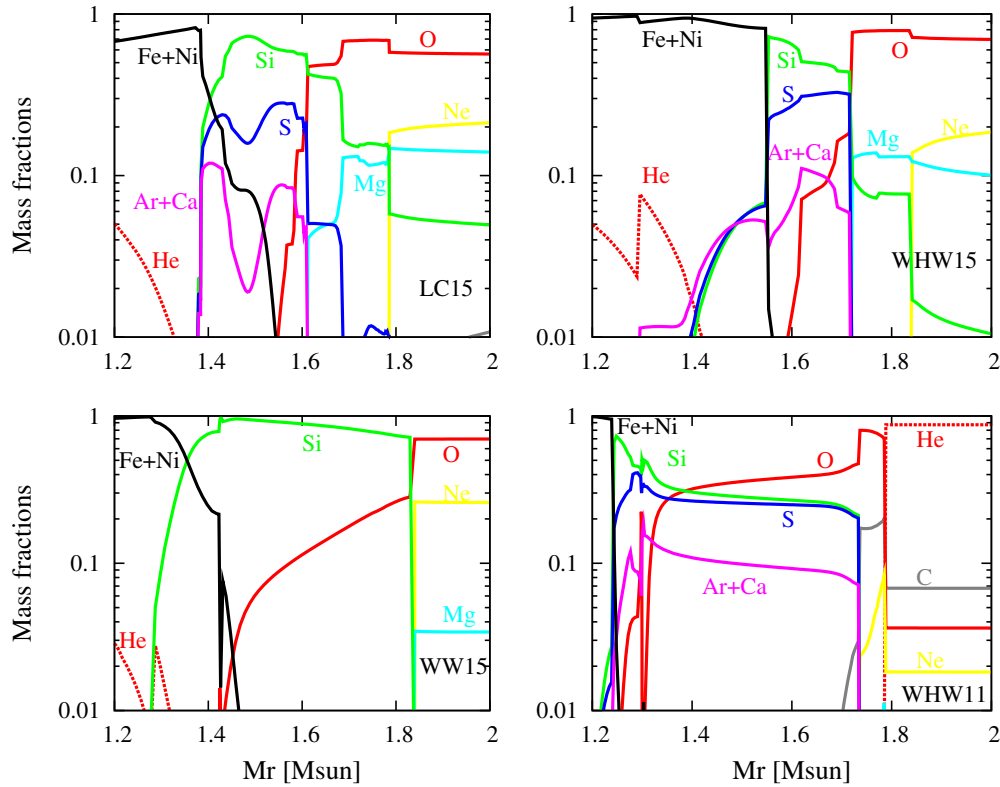
Figure 1. Pre-collapse composition distributions for the 15 $M_\odot$ stars of Limongi & Chieffi (2006; LC15, top left), Woosley & Weaver (1995; WW15, bottom left), and Woosley et al. (2002; WHW15, top right), and for the 11.2 $M_\odot$ star of Woosley et al. (2002; WHW11, bottom right).

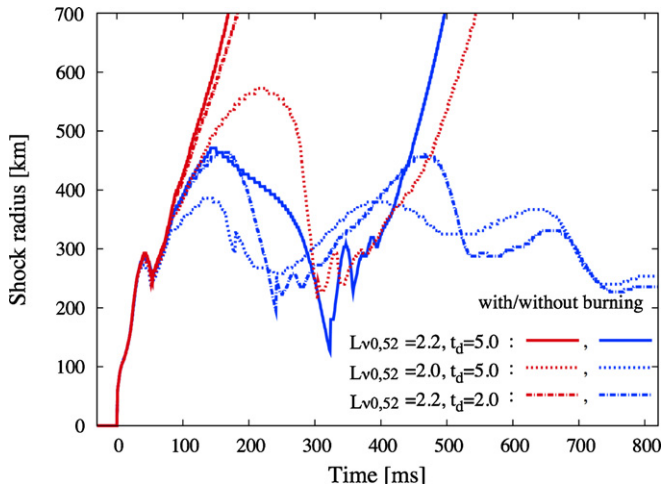(A color version of this figure is available in the online journal.)

Figure 2. Time evolution of the shock radii for model LC15 with different initial neutrino luminosities ($L_{\nu 0,52}$ in unit of 10^{52} erg s^{-1}) and the decay time (t_d in unit of s). The red and blue lines correspond to the results with and without the energy feedback from nuclear reactions, respectively.

(A color version of this figure is available in the online journal.)

on two parameters: the input neutrino luminosity $L_{\nu 0}$ and the decay time t_d (see Equation (6)).[9] We characterize models as $(L_{\nu 0,52}, t_d) = (x, y)$ for convenience, in which the luminosity and the decay time is $x \times 10^{52}$ (erg s^{-1}) and y (s), respectively.

　　Figure 2 shows comparisons of the postbounce shock evolution in 1D LC15 models depending on the two parameters

---

[9]　Without seeing a shock revival in ∼ 1 s postbounce, we call it "non-exploding" in this study.

$(L_{\nu 0,52}, t_d)$ and nuclear energy feedback from α network calculation. Three sets of parameters were chosen, $(L_{\nu 0,52}, t_d) = (2.2, 5.0)$, $(2.0, 5.0)$, and $(2.2, 2.0)$, and are shown as a solid line, a dotted line, and a dash-dotted line, respectively. All the models with nuclear burning, marked with red lines in Figure 2, present a shock expansion leading to explosions, whereas among the three models without nuclear burning (blue lines) only the model with relatively higher luminosity and longer decay time $((L_{\nu 0,52}, t_d) = (2.2, 5.0)$, solid blue line) exhibits a shock revival. Note that in all six cases in Figure 2, the bounce shock stalls and then transits to a passive shock, which presents negative radial velocity behind the shock. Only after the transition, the additional energy gain due to nuclear burning acts to bifurcate the path of the passive shock. Two of three models without burning (blue lines in Figure 2) experiences shock recession afterward, whereas the shock of the burning models (for red lines) expands with different revival timescales depending on the input neutrino parameters.

　　As seen in Figure 2, larger input neutrino luminosity and shorter decay timescale unsurprisingly leads to easier explosions. More importantly, by comparing the dotted red line with the dotted blue line $((L_{\nu 0,52}, t_d) = (2.0, 5.0))$, the shock is shown to shift from recession to expansion by the inclusion of nuclear burning. In the case of higher neutrino luminosity ($L_{\nu 0,52} = 2.2$), the trajectories of the shock are observed to be rather similar when the effect of nuclear burning is taken into account (compare the solid red with dashed red line).

　　In the following, we elaborate on how and why the shock expansion is affected by nuclear burning as observed in Figure 2. Figures 3 and 4 show the mass-shell trajectory of models LC15 with the different parameter set of $(L_{\nu 0,52}, t_d) = (2.2, 2.0)$, and
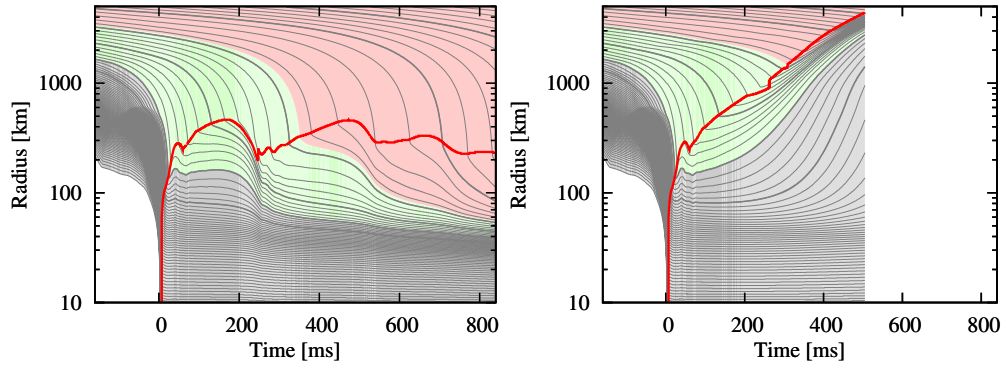
Figure 3. Evolution of model LC15 with a parameter set of $(L_{\nu0,52}, t_d) = (2.2, 2.0)$ visualized by the mass-shell trajectories. The thick red line starting at $t = 0$ denotes the position of the shock. Both cases, either without (left) or with (right) the energy feedback from nuclear reactions, are shown. The regions colored by gray, green, and red correspond to the iron, silicon, and oxygen layers, respectively. Thick gray lines correspond to the mass coordinates from 1.3 to 1.8 $M_\odot$ with every 0.1 $M_\odot$ (thin gray lines with every 0.02 $M_\odot$).

(A color version of this figure is available in the online journal.)
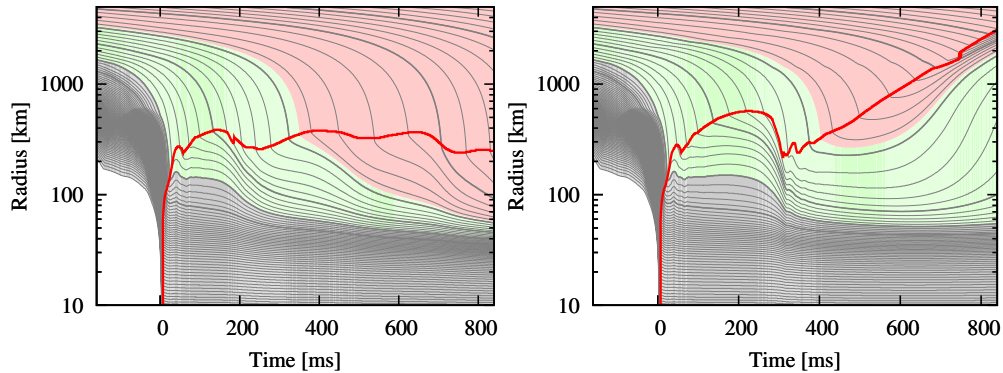
Figure 4. Same as Figure 3 but for the parameter set of $(L_{\nu0,52}, t_d) = (2.0, 5.0)$.

(A color version of this figure is available in the online journal.)

$(L_{\nu0,52}, t_d) = (2.0, 5.0)$, respectively. The former and latter case corresponds to the dashed and dotted line in Figure 2. Without nuclear burning (left panels in Figures 3 and 4), the stalled shock oscillates but does not turn into expansion (see also Figure 2). With nuclear burning (right panels of Figures 3 and 4), the shock expansion can be seen to take place when the shock front passes through the Si-rich layer (see the behavior of the thick red line in the green region in the right panel of Figure 3) or when it touches the O-rich layer (e.g., the shock in the red region in the right panel of Figure 4). For the latter case, the bounce shock firstly stalls, similar to the non-burning model (compare the left with the right panel in Figure 4), but the shock front deviates from the non-burning case when it encounters the O-rich layer.

For more detail about how the nuclear burning contributes to the shock acceleration, Figure 5 shows the radial velocity profiles and the composition distributions for model LC15 with the parameter set $(L_{\nu0,52}, t_d) = (2.2, 2.0)$ (which is the same parameter set as in Figure 3). At $t_{pb} = 150$ ms (top left panel), the shock front is in the progenitor Si-rich layer. Behind the shock front, heavier elements are synthesized as shown. The nuclear energy released by silicon burning heats the material behind the shock, giving it a small positive velocity (compare the velocity profiles with and without nuclear burning in the top left panel). The difference between the velocity profiles with versus without nuclear burning becomes outstanding when the O-rich layer starts to touch the shock front ($t_{pb} > 250$ ms). Figure 6

shows the evolution of the *diagnostic* (explosion) energy for burning (red line) and non-burning (blue line) cases as well as the net energy released via nuclear reactions (green line). As in Suwa et al. (2010), we define the *diagnostic* energy that refers to the integral of the energy over all zones that have a positive sum of the specific internal, kinetic, and gravitational energy. It is impossible to calculate the final energy of an explosion that is still occurring at this early post-bounce stage. After silicon burning starts to feed the energy behind the shock, in addition to neutrino heating (in the gain region, e.g., $t_{pb} = 150$ ms, see the top left panel in Figure 5), the diagnostic energy deviates from that without burning (compare the red and blue lines of Figure 6), which is also clearly visible in the shock evolution (Figure 3). From Figure 6, the total amount of 3.1×10^{50} erg is shown to be released through nuclear burning in this case, raising the diagnostic energy to 5.0×10^{50} erg.

As we already mentioned, oxygen burning predominantly triggers the shock expansion for the parameter set taken for Figure 4. In addition, the silicon layer is shown to be burned as a heating source (top left panel of Figure 7), which is the reason that the shock position becomes larger compared to the non-burning model (Figure 4). When the shock front begins to swallow the oxygen layer at ~400 ms postbounce (the right panel of Figure 4), the fresh fuel supplies energy to assist the shock expansion (see from top right, bottom left, to bottom right panels of Figure 7). If not for the energy gain, the stalled shock would not revive earlier than $t = 750$ ms, as seen from the
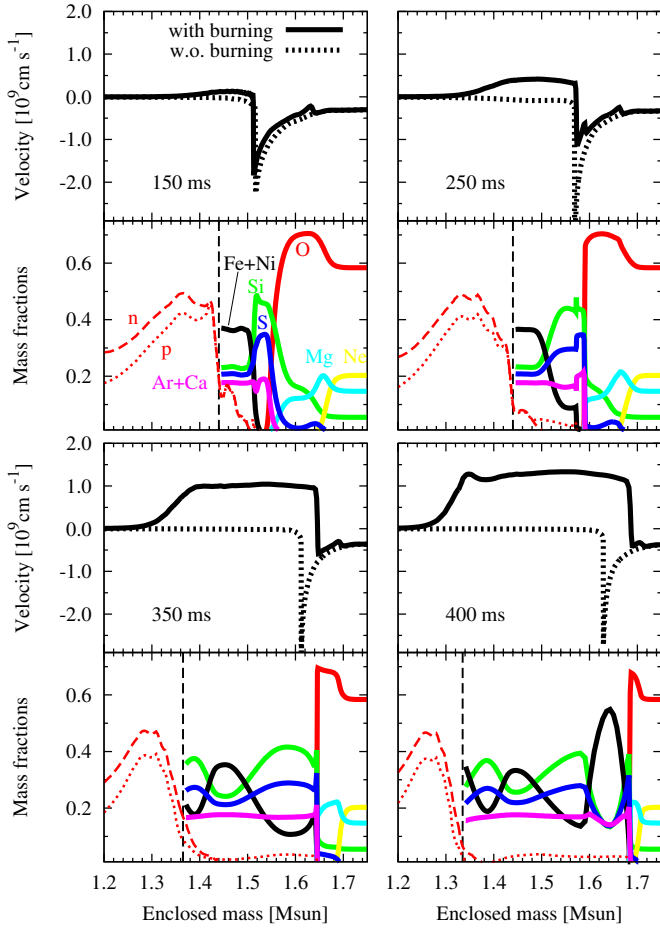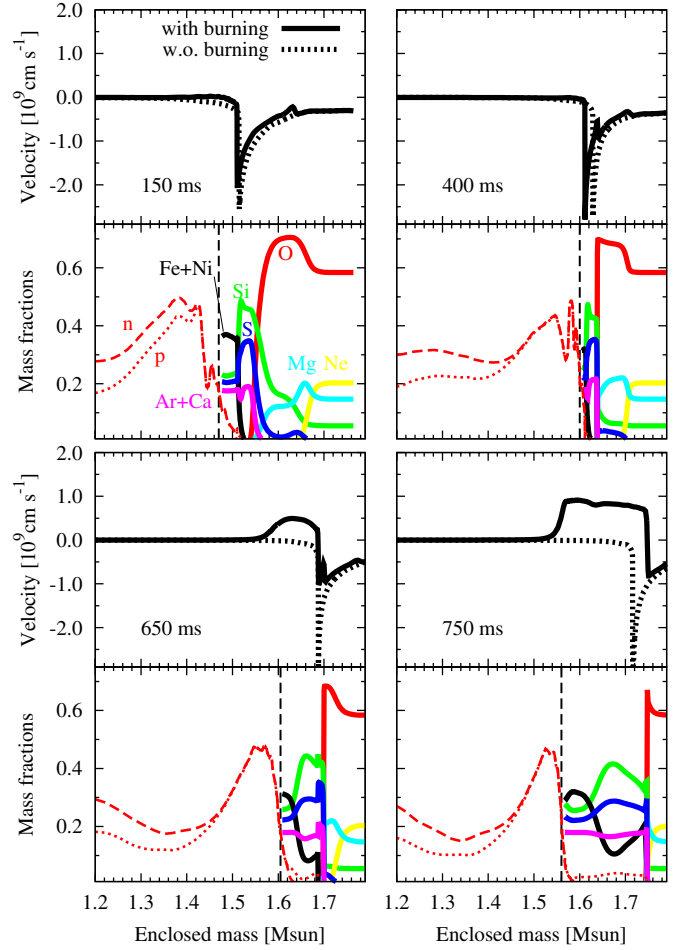
Figure 5. Snapshots of velocity profile (top) and composition distribution (bottom) for model LC15 with $(L_{\nu 0,52}, t_d) = (2.2, 2.0)$ at selected postbounce epochs (t_{pb} = 150, 250, 350, and 400 ms). Solid and dotted lines in the top of each panel show the velocity profile with or without nuclear burning, respectively. In the bottom part, distributions of representative elements of the burning model are shown. Note that the abundances of neutron (n) and proton (p) are estimated from Shen EOS and the others are calculated from the nuclear network calculation. The nucleon-rich region in the abundance plot is separated by a vertical dashed line.

(A color version of this figure is available in the online journal.)

Figure 7. Same as Figure 5 but for the parameter set of $(L_{\nu 0,52}, t_d) = (2.0, 5.0)$. (A color version of this figure is available in the online journal.)


Figure 6. Time evolution of diagnostic energy is shown for the same model as Figure 5. The green line is the energy released by nuclear burning and the diagnostic energy without nuclear burning (blue) is also shown. Here diagnostic energy is defined as the sum of the kinetic, thermal, and gravitational energy of fluid elements with positive radial velocity.

(A color version of this figure is available in the online journal.)
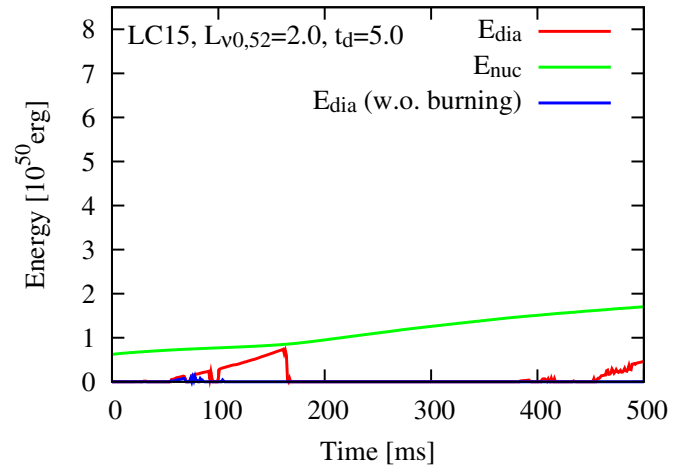
Figure 8. Same as Figure 6, but for the parameter set of $(L_{\nu 0,52}, t_d) = (2.0, 5.0)$. (A color version of this figure is available in the online journal.)

left panel of Figure 4. Even with the aid of nuclear burning, the explosion for this model (Figure 8) is weaker ($\lesssim 10^{50}$ erg) compared to the more luminous models (Figures 6 and 9). This suggests that nuclear burning has a secondary impact on the explosion mechanism—it can assist explosions only when the neutrino heating is working enough to push the weak shock to the fuel layers.
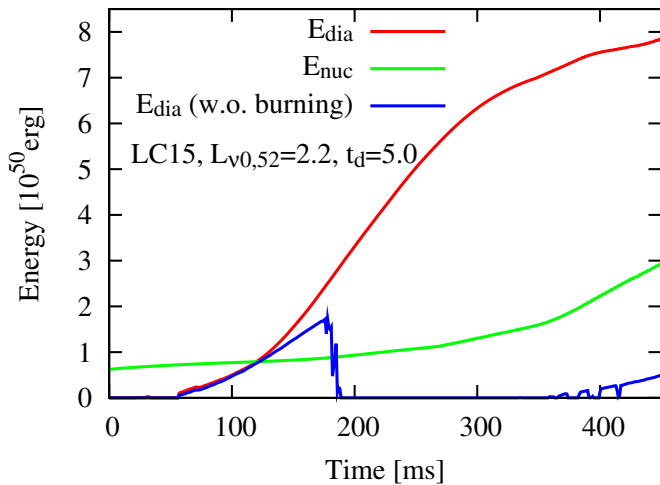
Figure 9. Same as Figure 6 but for the most energetic case, $(L_{\nu 0,52}, t_d) =$ (2.2, 5.0), among the three examples shown in Figure 2. The diagnostic energy with nuclear burning is about 8.0×10^{50} erg at $t_{pb} = 465$ ms and still keeps rising. The net energy released via nuclear reactions at this time is $\sim 3.0 \times 10^{50}$ erg, occupying a significant fraction ($\sim 40\%$) of the diagnostic energy. For the model without nuclear burning, the diagnostic energy is $\sim 0.8 \times 10^{50}$ erg at that time and closely saturates to be $E_{dia} \sim 2.3 \times 10^{50}$ erg afterward.

(A color version of this figure is available in the online journal.)

3.2. Progenitor Dependence

Figure 10 shows a parameter map on the $(L_{\nu 0,52}, t_d)$ plane for each progenitor. As can be seen, higher neutrino luminosity and/or longer decay time leads to easier explosions (colored by red and denoted as "Explosion"), whereas it is opposite for smaller neutrino luminosity and/or shorter decay time (colored

by light-blue and denoted as "No explosion" in the figure). For the LC15 progenitor model (top left panel), a parameter region colored by yellow can be seen between the exploding and the non-exploding regime, in which an explosion is obtained only when nuclear burning is included in the hydrodynamics simulations. The emergence of the yellow region means that the minimum neutrino luminosity necessary to drive an explosion is reduced by taking into account energy feedback from nuclear burning. The burning-mediated regime is clearly visible only for the LC15 progenitor. As already mentioned in Section 2.2, this is because this model possesses a massive oxygen layer and the oxygen shell is positioned closest to the center among the progenitors taken in this study.

The area of the yellow region in Figure 10 is not so large even for the LC15 progenitor, which suggests that nuclear burning has a secondary importance. In the case of energetic explosions, for example $(L_{\nu 0,52}, t_d) = (3.0, 0.8)$, a difference of diagnostic energy between models with and without nuclear burning is $\sim 5 \times 10^{49}$ erg (Table 2). For marginal weak explosions with $E_{dia} \lesssim 10^{50}$ erg (which are often the case in recent first-principle CCSN simulations), however, it should be emphasized that the inclusion of nuclear burning could increase the diagnostic energy up to about $\sim 0.6 \times 10^{51}$ erg.

The critical luminosity for explosions can be read from the y-axis in Figure 10 in the limit of long t_d (namely, approaching to a constant neutrino luminosity), which corresponds to 2.7 (WHW15), 2.0 (LC15), 1.9 (WW15), and 1.2 (WHW11) in unit of 10^{52} erg s^{-1}, respectively. The WHW15 model shows the highest critical neutrino luminosity among our models. This is because of the higher mass accretion rate of the WHW15 model (blue solid line in Figure 11), which makes the impact of nuclear burning relatively small. The critical luminos-
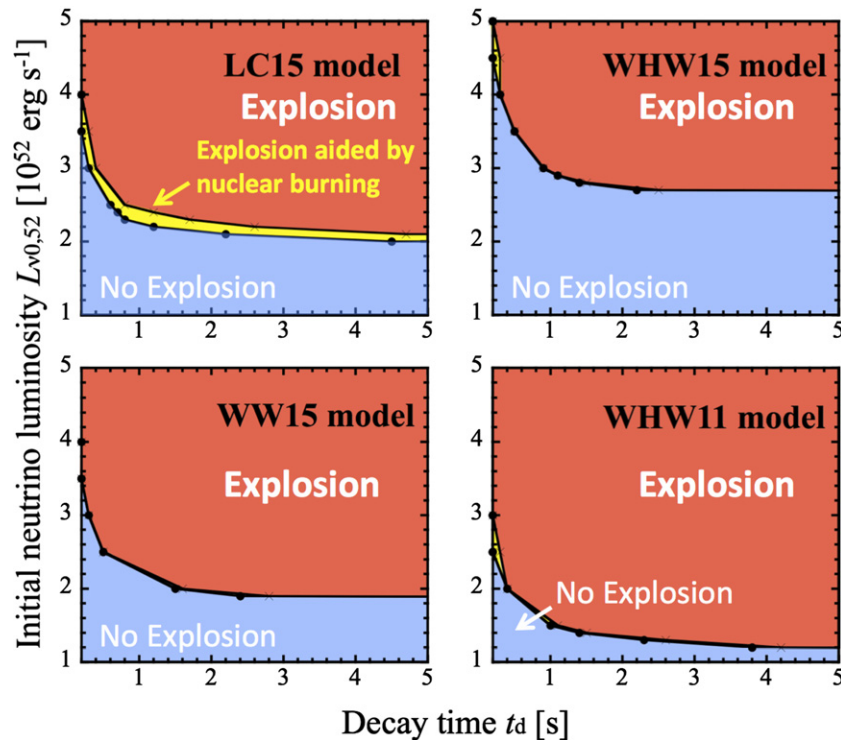

Figure 10. Parameter maps of the initial neutrino luminosity $L_{\nu 0,52}$ and its decay time t_d that separates the non-exploding regime (blue region) from the exploding one (red region) in 1D simulations for the four different progenitors. A horizontal yellow region inbetween (clearly visible for the LC15 progenitor; top left) shows the parameter region in which 1D explosions are obtained when the network calculation is performed.

(A color version of this figure is available in the online journal.)

Table 2
Summary of Results

Model	$L_{\nu 0,52}$ $(10^{52}\,\mathrm{erg\,s^{-1}})$	t_d (s)	Without Burning		With Burning	
			$t_{\exp}$ (s)	E_{dia} $(10^{51}\,\mathrm{erg})$	$t_{\exp}$ (s)	E_{dia} $(10^{51}\,\mathrm{erg})$
LC15	2.0	5.0	...	...	0.836	0.188
	2.2	2.0	...	...	0.502	0.516
	2.2	5.0	0.819	0.234	0.465	0.796
	2.5	0.8	0.811	0.065	0.460	0.359
	2.5	1.6	0.462	0.832	0.416	0.836
	3.0	0.4	0.498	0.140	0.424	0.203
	3.0	0.8	0.394	1.017	0.368	1.071
WHW15	2.7	2.5	0.712	0.765	0.598	0.906
	3.0	1.0	0.556	0.613	0.531	0.644
	3.5	0.5	0.493	0.379	0.477	0.403
	4.0	0.4	0.455	0.622	0.403	0.706
WW15	2.0	5.0	0.543	0.385	0.527	0.388
	3.0	1.0	0.360	1.058	0.357	1.087
	3.5	0.5	0.336	0.954	0.333	1.005
	4.0	0.3	0.325	0.651	0.322	0.704
WHW11	1.5	5.0	0.472	0.195	0.465	0.208
	2.0	5.0	0.353	0.821	0.349	0.845
	2.5	0.7	0.319	0.800	0.316	0.837
	3.0	0.4	0.292	0.911	0.289	0.951
LC15 (2D)	2.0	4.0	...	...	0.541	0.226
	2.2	2.0	0.664	0.113	0.491	0.301
	2.2	4.0	0.542	0.355	0.488	0.534
	2.5	0.8	0.596	0.099	0.461	0.237
	2.5	1.6	0.464	0.623	0.425	0.692
	3.0	0.4	0.514	0.019	0.437	0.151
	3.0	0.8	0.401	0.881	0.372	0.947
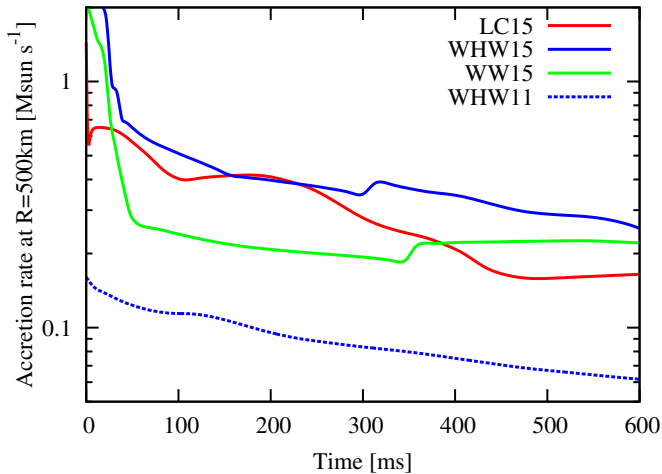
Figure 11. Time evolution of the mass accretion rates, evaluated at $R = 500\,\mathrm{km}$, for four non-exploding models.

(A color version of this figure is available in the online journal.)

ity becomes smallest for model WHW11, mainly owing to the compactness of the pre-collapse core and small mass accretion rate coming from its tenuous envelope, as shown in a blue dotted line in Figure 11. The mass accretion rate, averaged between 200 ms and 600 ms after bounce for each model, is 0.33 (WHW15), 0.23 (LC15), 0.21 (WW15), and 0.08 $M_\odot\,\mathrm{s^{-1}}$ (WHW11), respectively, which is roughly proportional to the critical luminosity except for the WHW11 progenitor model. When the input luminosity is taken below the critical curves, nuclear burning cannot drive explosions alone

because the shock needs to expand far away from the central protoneutron star by neutrino heating (i.e., the shock revival due to neutrino heating is preconditioned to enjoy the assistance from nuclear burning).

In Table 2, the time of explosion, $t_{\exp}$, and diagnostic energy, E_{dia}, are listed for some chosen sets of the neutrino parameters. The time of explosion is defined as the moment when a shock reaches an average radius of 4500 km, while non-exploding models are denoted by a "—" symbol. The diagnostic energy is plotted as a function of neutrino luminosity for a various decay time scale in Figure 12. In fact, the diagnostic energy is shown to be remarkably enhanced in the case of marginal explosions (i.e., low neutrino luminosity $L_{\nu,0}$ and/or short decay time t_d), and the difference gets smaller for large $L_{\nu,0}$ and t_d, in which explosions are predominantly triggered by neutrino heating. As previously mentioned, these features, which are due to nuclear burning, are only remarkable in the LC15 progenitor. Nevertheless, it is worth mentioning that even for the WW95 progenitor the shock extent, for which the impact of nuclear burning is relatively small (see the bottom left panel of Figure 10), becomes bigger for models with nuclear burning compared to those without (Figure 13).

3.3. 2D Results

We move on to discuss axi-symmetric 2D models and examine the effects of nuclear burning in the same manner as in the previous section. To clearly see the impacts of nuclear burning in our 2D simulations, we choose to employ the LC15 in the following.

Figures 14 and 15 show entropy evolution (left-hand side in each panel) with the mass fraction of silicon (right-hand
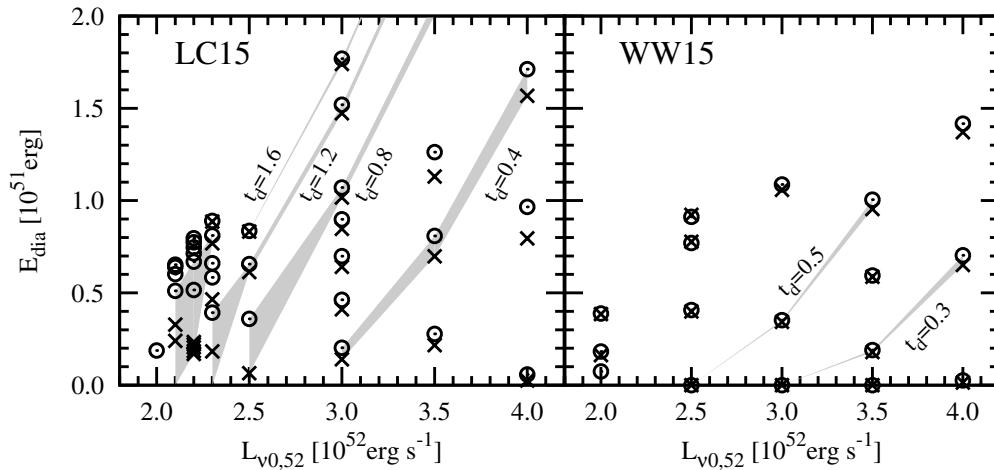
Figure 12. Diagnostic energy as a function of initial neutrino luminosity $L_{\nu 0,52}$. The shaded area shows the energy difference between the models with (open circles) and without nuclear burning (crosses) for some selected t_d sequences. Left: the case of LC15 progenitor. It can be seen that energy difference tends to be large for less energetic models. Right: the case of WW15 progenitor. The energy difference is small even for less energetic models.
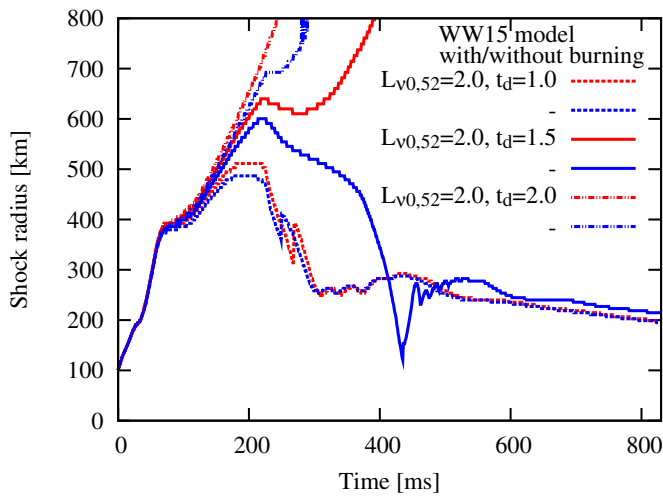

Figure 13. Time evolution of the shock radii for several 1D models employing the WW15 progenitor. The shock moves farther out for models including nuclear burning (red lines) compared to those without (blue).

(A color version of this figure is available in the online journal.)

side) for two sets of neutrino parameters at selected postbounce epochs ($t_{pb} = 100$ and 200 ms postbounce). Small- and large-scale inhomogeneities in the entropy plots come from neutrino-driven convection and the SASI, both of which lead to more easier explosions in 2D than 1D (e.g., Marek & Janka 2009; Murphy & Burrows 2008; Ohnishi et al. 2006).

Reflecting the stochastic motions of the expanding shocks, the way the (anisotropic) shock surfaces touch the nuclear fuel (in the shape of spherical shells) changes from model to model in 2D. In the case of $L_{\nu 0,52} = 2.4$ (Figure 14), the expanding shock first reaches to the silicon layer near in the vicinity of the north pole at $t \sim 150$ ms. Simultaneously, heavy elements like nickel are synthesized, which helps to push the burning material preferentially along the direction. In a less luminous case, assuming smaller luminosity ($L_{\nu 0,52} = 2.2$) and the same decay time (Figure 15), the shock encounters the silicon layer closer to the center, where a mass accretion rate is effectively higher, resulting in the longer explosion time.

As shown from Figure 16, nuclear burning does assist 2D explosions similar to 1D, but the energy difference (here

$\sim 0.2 \times 10^{51}$ erg) is generally smaller in 2D than in 1D (compare with Figures 6 and 9). The comparison of the energy gain due to nuclear burning between 1D and 2D models is more clearly shown in Table 2 and Figure 17. The difference of the diagnostic energy with and without nuclear burning is larger in 1D than in 2D. This may be because neutrino-driven convection and the SASI in 2D models (as indicated by entropy distributions in Figures 14 and 15) enhances the neutrino heating efficiency, which makes the contribution of nuclear burning relatively smaller compared to 1D models.

Finally Figure 18 is the parameter map in 2D for the LC15 progenitor. As expected, 2D hydrodynamics leads to easier explosions compared to 1D (see the dashed lines that are the critical curves in 1D). More importantly, the yellow region still exists in 2D models for the LC15 progenitor. Nuclear energy released in 2D models reduces the critical luminosity by $0.1–0.5 \times 10^{52}$ erg s^{-1} depending on t_d, as well as 1D models, although its impact on the diagnostic energy is weaker than for 1D models. It would be interesting to perform multi-D (radiation-hydro) simulations with a nuclear network calculation for the previously untested progenitor model.

4. CONCLUSIONS

We revisited the potential impacts of nuclear burning on the onset of neutrino-driven explosions of CCSNe. By changing the neutrino luminosity and its decay time to obtain parametric explosions in 1D and 2D models with or without a 13 isotope α network, we studied how the inclusion of nuclear burning could affect the postbounce dynamics for four progenitor models: three for 15.0 $M_\odot$ stars of Limongi & Chieffi (2006), Woosley & Weaver (1995), and Woosley et al. (2002), and one for an 11.2 $M_\odot$ star of Woosley et al. (2002). Our results showed that the energy gain due to the nuclear burning of infalling material behind the shock can energize the shock expansion, especially for models that produce only marginal explosions in the absence of nuclear burning. These models enjoy assistance from nuclear burning, typically in the following two ways: whether the shock front passes through the silicon-rich layer, or later when it touches the oxygen-rich layer. Depending on the neutrino luminosity and its decay time, the diagnostic energy of the explosion was found to increase up to a few times 10^{50} erg for models with nuclear burning, compared to the
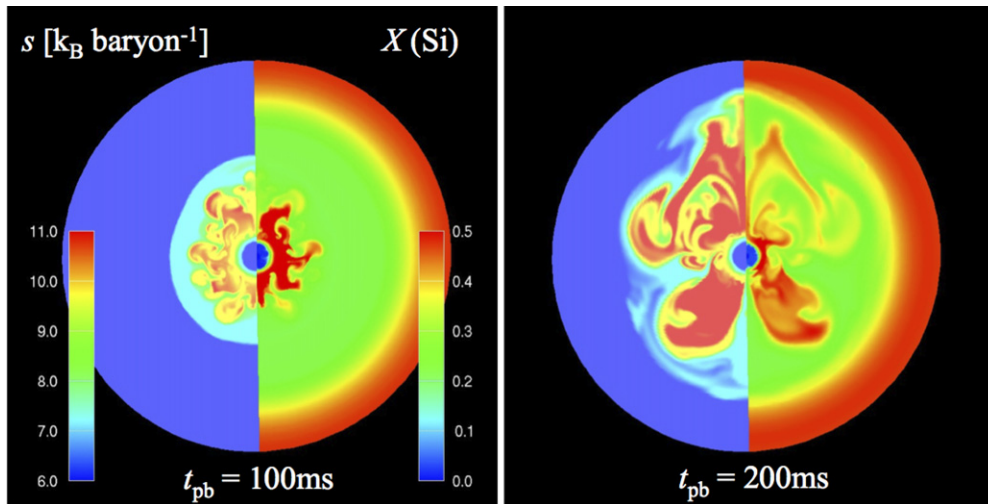
Figure 14. 2D distributions of entropy and silicon of LC15 model ($n_\theta = 128$). Entropy in unit of k_B baryon^{-1} is in the left half of the sphere and the silicon mass fraction is in the right half. Shown is the case of $(L_{\nu0,52}, t_d) = (2.4, 1.1)$ at $t_{pb} = 100$ (left panel) and 200 ms (right) postbounce, respectively.
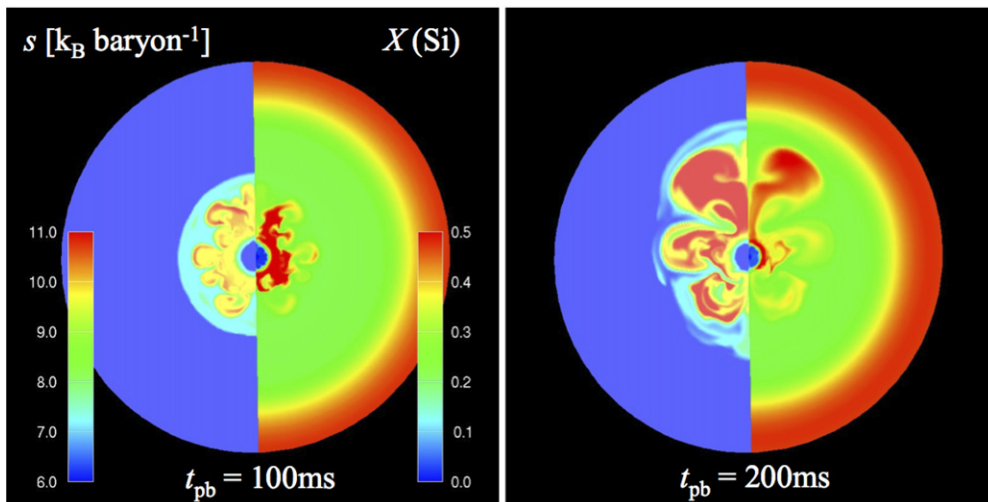(A color version of this figure is available in the online journal.)

Figure 15. Same as Figure 14 but of a 2D model with $(L_{\nu0,52}, t_d) = (2.2, 1.1)$.
(A color version of this figure is available in the online journal.)

corresponding models without. The energy difference becomes generally smaller in 2D than in 1D because neutrino-driven convection and the SASI in 2D models enhances the neutrino heating efficiency, making the contribution of nuclear burning relatively smaller compared to 1D models. These features are most remarkable for the LC15 progenitor, which possesses a massive oxygen layer with its inner-edge radius being smallest among the employed progenitors. This makes the timescale shorter for the shock to encounter the rich fuel. Considering reduction of the critical luminosity and increase of the diagnostic energy by nuclear burning, as well as uncertainties in the structure of progenitors, our results indicate that nuclear burning should still remain one of the important ingredients to foster the onset of neutrino-driven explosions.

APPENDIX A

α NETWORK VERSUS FLASHING METHOD

In this paper, we use a reaction network involving 13 α nuclei for the purpose of investigating the potential role of nuclear burning in reviving and strengthening weak shocks in neutrino-driven explosions. Although the 13 α network calculation itself is rather simple, it is computationally expensive to perform them for each species evolved with multi-D hydrodynamics. To
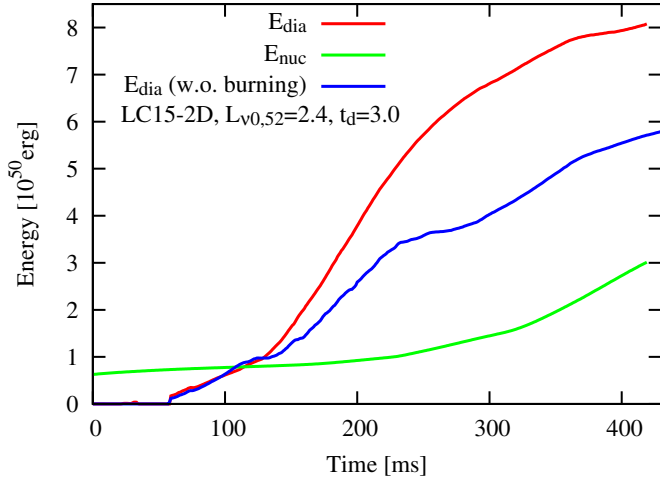
Figure 16. Time evolution of the diagnostic energy (red line) and net nuclear burning energy (green) for LC15 model in 2D ($n_\theta = 32$) with ($L_{\nu 0,52}, t_d$) = (2.4, 3.0). The diagnostic energy of the case without nuclear burning (blue) is also shown.

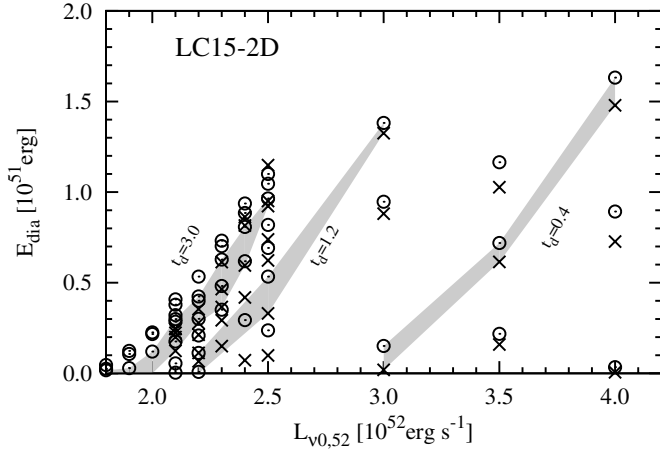(A color version of this figure is available in the online journal.)

Figure 17. Same as Figure 12 but for LC15 model in 2D ($n_\theta = 32$).
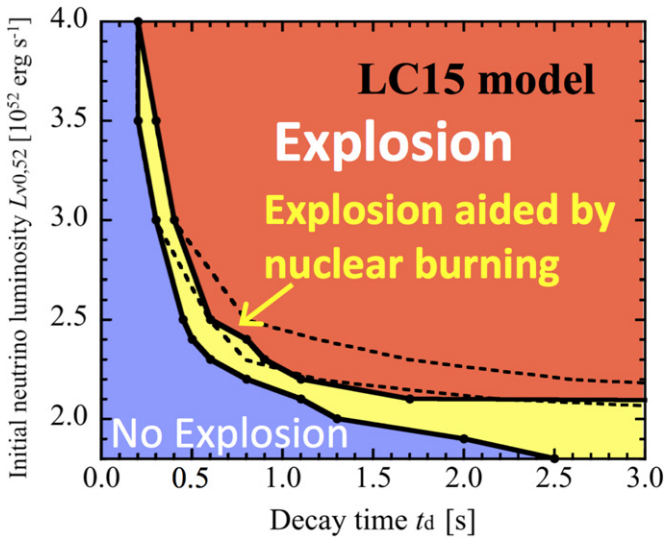

Figure 18. Same as Figure 10 but for 2D simulations. The dashed lines represent the critical curves in 1D (compare Figure 10). Note that we adopt coarse mesh points in the polar direction (32 uniform grids), so that we can perform 2D simulations for 174 models in total to make this parameter map.

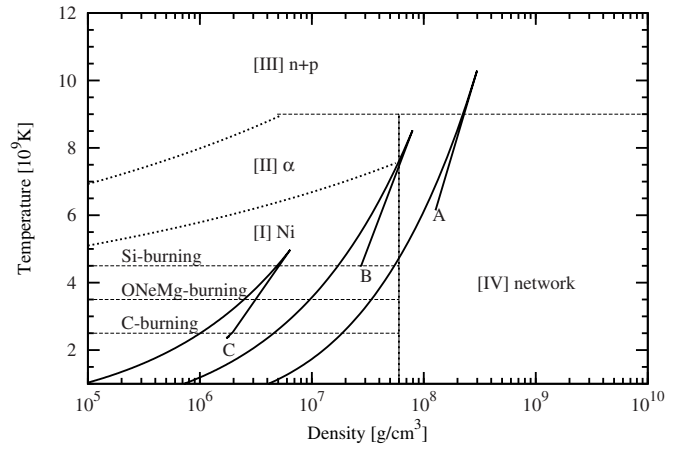(A color version of this figure is available in the online journal.)

Figure 19. Schematic picture of ρ–T plane characterizing our pseudo-flashing method. Region I almost consists of nickel, region II contains α-particles and free nucleons, and in region III all nuclei and α-particles are dissolved into free nucleons. In region IV we resolve the nuclear network to evolve the chemical compositions. See Rampp & Janka (2002) for details. We take three flows (A, B, and C) as representations of mass shells in the LC15 model.

avoid this, various simplifications are employed, for example, a "flashing method" (Rampp & Janka 2002). In the flashing method, a hydrodynamic flow is characterized by its matter density ρ and temperature T. The flow travels in a ρ–T plane, changes its chemical composition, and releases nuclear energy according to the region where it is in the plane. Figure 19 presents the composition of flows in the ρ–T plane, which is slightly different from the original (Rampp & Janka 2002). We compare the evolution of the composition and subsequent energy release of flows in this "pseudo-" flashing method with those in our α network.

Following Rampp & Janka (2002) we assume that the dissociation of nuclei and the recombination of free nucleons and α-particles change the chemical composition below the transition density ($\rho_0 = 6 \times 10^7 \,\mathrm{g\,cm^{-3}}$). In region I all free nucleons and α particles form ^{56}Ni. In region II all heavy nuclei are dissolved and free nucleons recombine into α particles. In region III all heavy nuclei and α particles are disintegrated into free nucleons. These three regions are separated by two curves $\rho_1(T)$, $\rho_2(T)$ in the ρ–T plane:

$$\log_{10}(\rho_1(T)) = 11.62 + 1.5\log_{10}(T_9) - 39.17/T_9, \quad \text{(A1)}$$

$$\log_{10}(\rho_2(T)) = 10.60 + 1.5\log_{10}(T_9) - 46.54/T_9, \quad \text{(A2)}$$

where T_9 is the temperature in unit of 10^9 K. Above the transition density (region IV) we calculate the nuclear network instead of using the EOS of Lattimer & Swesty (1991) as in Rampp & Janka (2002). Three horizontal lines at $T_9 = 2.5$, 3.5, and 4.5 present ^{12}C burning to ^{24}Mg, ^{16}O–^{20}Ne–^{24}Mg burning to ^{28}Si, and ^{28}Si burning to ^{56}Ni, respectively. At $T_9 > 9$ we assume that all nuclei are disintegrated into free nucleon independent of density.

Here we take three flows in the LC15 model, which we named A, B, and C, located in the mass coordinate at 1.3 $M_\odot$ (Fe core), 1.5 $M_\odot$ (Si layer), and 1.7 $M_\odot$ (O/Si layer), respectively. These flows are launched via 1D hydrodynamic simulation by putting thermal energy in the innermost region of the iron core so that the explosion energy of 10^{51} erg is obtained. Each flow undergoes shock heating and compression (to the upper right direction in Figure 19), and then expands and gets cool (to the
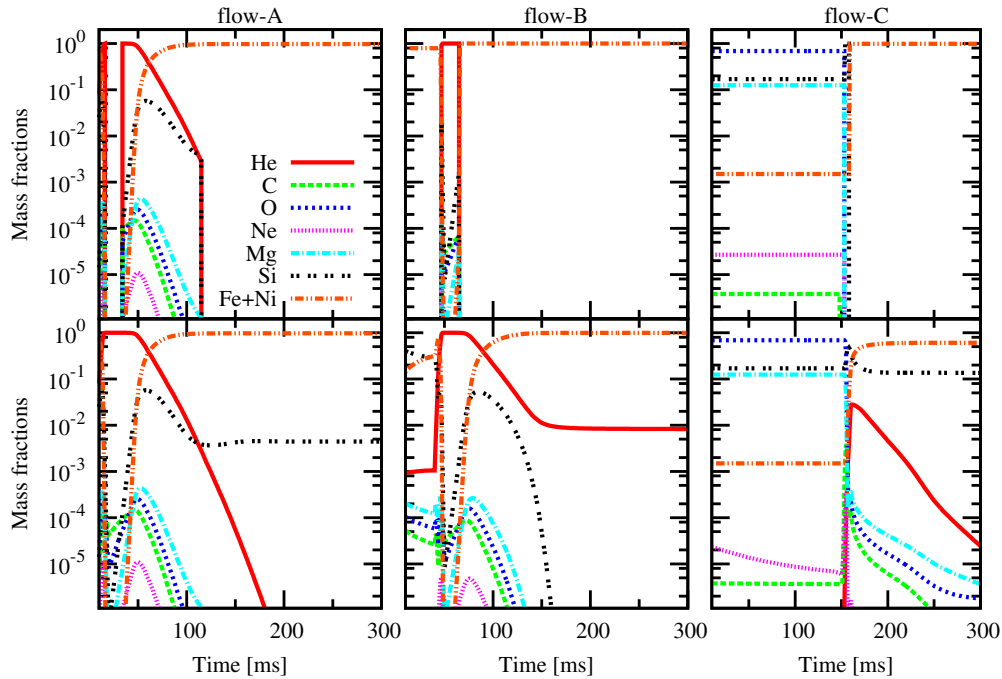
Figure 20. Time evolution of chemical compositions of flow A, B, and C. The results from the pseudo-flashing method (top panels) and network calculation (bottom) are shown.

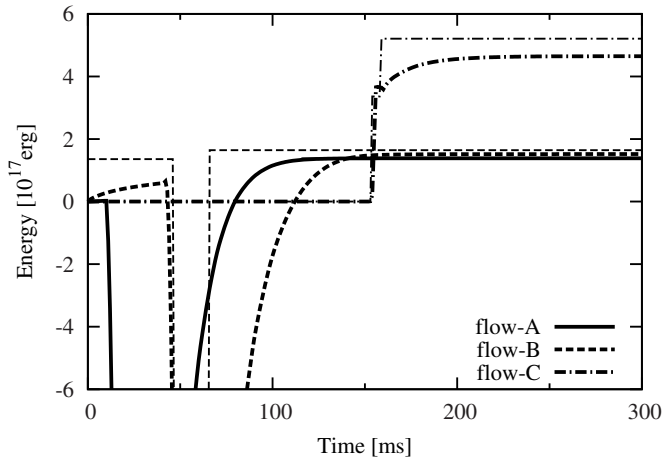(A color version of this figure is available in the online journal.)

Figure 21. Temporal summations of released energy through nuclear reactions. Results from the network calculation (thick lines) and pseudo-flashing method (thin lines) are shown for three flows. The solid thin line (flow-A calculated with the pseudo-flashing method) presents almost the same evolution as the network case and is hidden by the solid thick line.

lower left). We compare the change of chemical compositions (Figure 20) and released energy (Figure 21) via the flashing method with those estimated by α network. Both methods show a similar energy yield for all flows at the late phase, although the intermediate evolution and final abundance of intermediate-mass elements are different. This difference is caused by our treatment that the composition immediately changes when a flow goes across a line separating regions presented in Figure 19. To avoid the unrealistic jump, Rampp & Janka (2002) introduced factors f_I, f_{II}, and f_{III} so that the composition change progresses gradually. We conclude that the flashing method is a good approximation and useful for SN simulations.

APPENDIX B

LIGHT-BULB SCHEME VERSUS ISOTROPIC DIFFUSION SOURCE APPROXIMATION

Our current study is based on the light-bulb (LB) scheme, in which a prescribed neutrino heating and cooling rate is used. This simple approach reduces computational cost compared with more sophisticated simulations and makes our extensive parameter study possible. The LB approximation has been used for various purposes, such as studying the effects of spacial dimensionality (e.g., Dolence et al. 2013; Couch 2013b) and progenitor inhomogeneities (Couch & Ott 2013) on the neutrino-driven mechanism, explosive nucleosynthesis (e.g., Fujimoto et al. 2011), gravitational wave signals (e.g., Kotake et al. 2009a, 2009b, 2011), and so on. The LB method is also useful for removing feedback from physical inputs into the neutrino luminosity and temperature, which enables us to investigate the relative changes due to the different choice of the physical inputs (e.g., EOS study by Couch 2013a).

In this appendix, we briefly discuss the validity of the LB scheme by comparing the neutrino luminosities, average energy, and heating rates assumed in this study with those from 1D simulations in which spectral neutrino transport is solved by the isotropic diffusion source approximation (IDSA) scheme (see Liebendörfer et al. 2009 for more details). We employ the LC15 progenitor model in both of the two runs. Figure 22 shows the time evolution of neutrino luminosities estimated from IDSA simulations. In previous studies using the LB models, the neutrino luminosities are assumed to be constant, although it is apparently unrealistic. In this paper we introduced another parameter, the decay time of neutrino luminosities, to complement this discrepancy. The neutrino luminosities are not a monotonic function of time and only a late phase can be fit by an exponential decay with $t_d = 0.3$ s. The evolution of the average energy of neutrinos is shown in Figure 23.
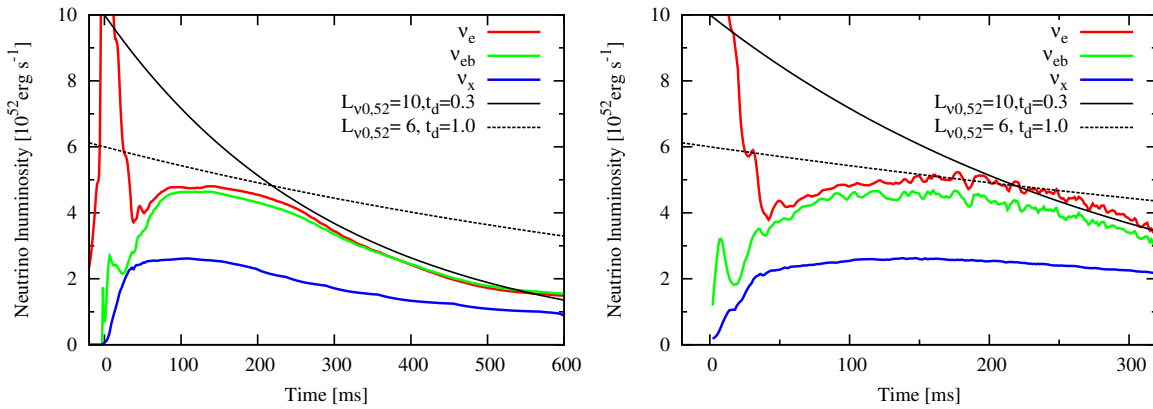
Figure 22. Neutrino luminosity resulting from IDSA simulations of 1D (left) and 2D (right) for LC15 model.

(A color version of this figure is available in the online journal.)
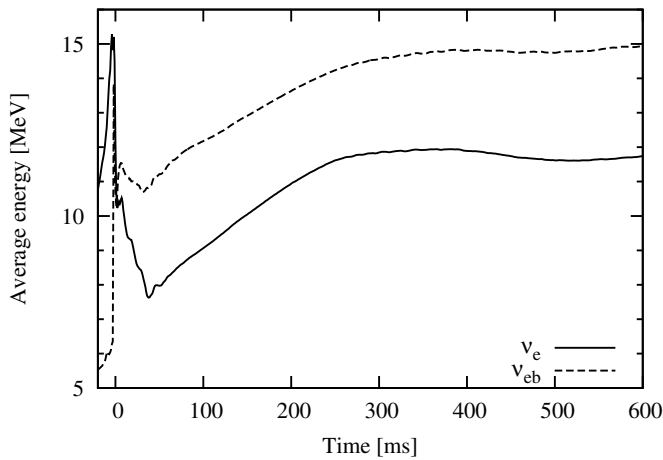

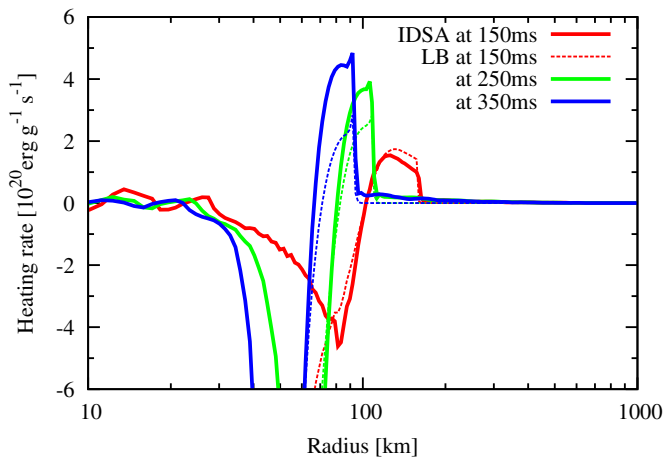**Figure 23.** Time evolution of neutrino energy for 1D model.

Figure 24. Radial distribution of heating rates for 1D model at $t_{pb} = 150$ (red lines), 250 (green lines), and 350 ms (blue lines). LB models (thin lines) tend to overestimate the heating rate in a pre-shock region and underestimate in a post-shock region.

(A color version of this figure is available in the online journal.)

According to previous studies, we assume the electron neutrino temperature to be constant at 4 MeV. Figure 23 presents an almost constant energy of neutrinos with $E_{\nu_e} \sim 12$ MeV, indicating that the constant neutrino temperature is not a bad assumption. Finally we compare the neutrino heating rate from the IDSA simulations with that from the LB scheme (Figure 24).

Taking the neutrino luminosity, electron and neutron fractions, and temperature distributions from the IDSA simulation, we put them into Equations (4) and (5) to estimate the heating rate by the LB scheme. Note that we drop a suppression term $e^{\tau_{\nu_e}}$ for the current estimation. The LB model captures the heating and cooling regions well, although the heating rate behind the shock is underestimated compared to that from IDSA. Nevertheless, it is still a powerful tool for a parametric search to explore qualitative trends, such as the effects of neutrino luminosity, its decay timescale, and nuclear burning on boosting the onset of neutrino-driven explosions.

REFERENCES

Angulo, C., Arnould, M., Rayet, M., et al. 1999, NuPhA, 656, 3
Arcones, A., & Janka, H.-T. 2011, A&A, 526, A160
Arcones, A., Martínez-Pinedo, G., O'Connor, E., et al. 2008, PhRvC, 78, 015806
Audi, G., & Wapstra, A. H. 1995, NuPhA, 595, 409
Bethe, H. A., & Wilson, J. R. 1985, ApJ, 295, 14
Blondin, J. M., Mezzacappa, A., & DeMarino, C. 2003, ApJ, 584, 971
Bruenn, S. W., Dirk, C. J., Mezzacappa, A., et al. 2006, JPhCS, 46, 393
Bruenn, S. W., Mezzacappa, A., Hix, W. R., et al. 2009, JPhCS, 180, 012018
Bruenn, S. W., Mezzacappa, A., Hix, W. R., et al. 2013, ApJL, 767, L6
Buras, R., Janka, H.-Th., Rampp, M., & Kifonidis, K. 2006a, A&A, 457, 281
Buras, R., Rampp, M., Janka, H.-Th., & Kifonidis, K. 2006b, A&A, 447, 1049
Burrows, A., Dessart, L., Livne, E., Ott, C. D., & Murphy, J. 2007, ApJ, 664, 416
Burrows, A., & Goshy, J. 1993, ApJL, 416, L75
Burrows, A., Hayes, J., & Fryxell, B. A. 1995, ApJ, 450, 830
Burrows, A., Livne, E., Dessart, L., Ott, C. D., & Murphy, J. 2006, ApJ, 640, 878
Colgate, S. A., & White, R. H. 1966, ApJ, 143, 626
Couch, S. M. 2013a, ApJ, 765, 29
Couch, S. M. 2013b, ApJ, 775, 35
Couch, S. M., & Ott, C. D. 2013, ApJL, 778, L7
Dolence, J. C., Burrows, A., Murphy, J. W., & Nordhaus, J. 2013, ApJ, 765, 110
Endeve, E., Cardall, C. Y., Budiardja, R. D., et al. 2012, ApJ, 751, 26
Fernández, R. 2010, ApJ, 725, 1563
Fernández, R., Mueller, B., Foglizzo, T., & Janka, H.-T. 2013, arXiv:1310.0469
Fernández, R., & Thompson, C. 2009a, ApJ, 703, 1464
Fernández, R., & Thompson, C. 2009b, ApJ, 697, 1827
Foglizzo, T., Galletti, P., Scheck, L., & Janka, H.-T. 2007, ApJ, 654, 1006
Foglizzo, T., Masset, F., Guilet, J., & Durand, G. 2012, PhRvL, 108, 051103
Foglizzo, T., Scheck, L., & Janka, H.-Th. 2006, ApJ, 652, 1436
Fryer, C. L. 2004, ApJL, 601, L175
Fryer, C. L., Holz, D. E., & Hughes, S. A. 2002, ApJ, 565, 430
Fujimoto, S.-i., Kotake, K., Hashimoto, M.-a., Ono, M., & Ohnishi, N. 2011, ApJ, 738, 61
Guilet, J., Foglizzo, T., & Fromang, S. 2011, ApJ, 729, 71
Hammer, N. J., Janka, H.-T., & Müller, E. 2010, ApJ, 714, 1371
Hanke, F., Marek, A., Müller, B., & Janka, H.-T. 2012, ApJ, 755, 138
Hanke, F., Müller, B., Wongwathanarat, A., Marek, A., & Janka, H.-T. 2013, ApJ, 770, 66

Haxton, W. C. 1988, PhRvL, 60, 1999
Hayes, J. C., Norman, M. L., Fiedler, R. A., et al. 2006, ApJS, 165, 188
Herant, M., Benz, W., & Colgate, S. 1992, ApJ, 395, 642
Iwakami, W., Kotake, K., Ohnishi, N., Yamada, S., & Sawada, K. 2008, ApJ, 678, 1207
Iwakami, W., Kotake, K., Ohnishi, N., Yamada, S., & Sawada, K. 2009, ApJ, 700, 232
Janka, H.-T. 2012, ARNPS, 62, 407
Janka, H.-T., Kifonidis, K., & Rampp, M. 2001, in Lecture Notes in Physics, Physics of Neutron Star Interiors, Vol. 578, ed. D. Blaschke, N. K. Glendenning, & A. Sedrakian, 363
Janka, H.-T., & Müller, E. 1996, A&A, 306, 167
Janka, H.-Th. 2001, A&A, 368, 527
Kifonidis, K., Plewa, T., Janka, H.-T., & Müller, E. 2003, A&A, 408, 621
Kotake, K. 2013, CRPhy, 14, 318
Kotake, K., Iwakami, W., Ohnishi, N., & Yamada, S. 2009a, ApJL, 697, L133
Kotake, K., Iwakami, W., Ohnishi, N., & Yamada, S. 2009b, ApJ, 704, 951
Kotake, K., Iwakami-Nakano, W., & Ohnishi, N. 2011, ApJ, 736, 124
Kotake, K., Sato, K., & Takahashi, K. 2006, RPPh, 69, 971
Kotake, K., Sawai, H., Yamada, S., & Sato, K. 2004a, ApJ, 608, 391
Kotake, K., Sumiyoshi, K., Yamada, S., et al. 2012, PTEP, 2012, 01A301
Kotake, K., Takiwaki, T., Suwa, Y., et al. 2012c, AdAst, 2012, 428757
Kotake, K., Yamada, S., & Sato, K. 2003, ApJ, 595, 304
Kotake, K., Yamada, S., Sato, K., et al. 2004b, PhRvD, 69, 124004
Kuroda, T., Kotake, K., & Takiwaki, T. 2012, ApJ, 755, 11
Kuroda, T., Takiwaki, T., & Kotake, K. 2013, arXiv:1304.4372
Langanke, K., Martínez-Pinedo, G., Müller, B., et al. 2008, PhRvL, 100, 011101
Lattimer, J. M., & Lim, Y. 2013, ApJ, 771, 51
Lattimer, J. M., & Swesty, F. D. 1991, NuPhA, 535, 331
Lentz, E. J., Mezzacappa, A., Bronson Messer, O. E., et al. 2012a, ApJ, 747, 73
Lentz, E. J., Mezzacappa, A., Bronson Messer, O. E., Hix, W. R., & Bruenn, S. W. 2012b, ApJ, 760, 94
Liebendörfer, M. 2005, ApJ, 633, 1042
Liebendörfer, M., Mezzacappa, A., Thielemann, F.-K., et al. 2001, PhRvD, 63, 103004
Liebendörfer, M., Whitehouse, S. C., & Fischer, T. 2009, ApJ, 698, 1174
Limongi, M., & Chieffi, A. 2006, ApJ, 647, 483
Marek, A., & Janka, H.-Th. 2009, ApJ, 694, 664
Marek, A., Janka, H.-T., & Müller, E. 2009, A&A, 496, 475
Mezzacappa, A., Bruenn, S. W., Blondin, J. M., Hix, W. R., & Bronson Messer, O. E. 2007, in AIP Conf. Ser. 924, The Multicolored Landscape of Compact Objects and Their Explosive Origins, ed. T. diSalvo, G. L. Israel, L. Piersant et al. (Melville, NY: AIP), 234
Müller, B., Janka, H.-T., & Heger, A. 2012a, ApJ, 761, 72
Müller, B., Janka, H.-T., Marek, A., et al. 2011, in DESY Proceedings Series, Hamburg Neutrinos from Supernova Explosions, 14
Müller, B., Janka, H.-T., & Marek, A. 2012b, ApJ, 756, 84
Müller, B., Janka, H.-T., & Marek, A. 2013, ApJ, 766, 43
Murphy, J. W., & Burrows, A. 2008, ApJ, 688, 1159
Nakamura, S. X., Sumiyoshi, K., & Sato, T. 2009, PhRvC, 80, 035802
Nordhaus, J., Burrows, A., Almgren, A., & Bell, J. 2010, ApJ, 720, 694
Obergaulinger, M., & Janka, H.-T. 2011, arXiv:1101.1198
Ohnishi, N., Kotake, K., & Yamada, S. 2006, ApJ, 641, 1018
Ohnishi, N., Kotake, K., & Yamada, S. 2007, ApJ, 667, 375
Ott, C. D., Burrows, A., Dessart, L., & Livne, E. 2008, ApJ, 685, 1069
Sagert, I., Fischer, T., Hempel, M., et al. 2009, PhRvL, 102, 081101
Scheck, L., Kifonidis, K., Janka, H., & Müller, E. 2006, A&A, 457, 963
Scheck, L., Plewa, T., Janka, H.-T., Kifonidis, K., & Müller, E. 2004, PhRvL, 92, 011103
Shen, H., Toki, H., Oyamatsu, K., & Sumiyoshi, K. 1998, NuPhA, 637, 435
Steiner, A. W., Lattimer, J. M., & Brown, E. F. 2010, ApJ, 722, 33
Sumiyoshi, K., & Röpke, G. 2008, PhRvC, 77, 055804
Sumiyoshi, K., & Yamada, S. 2012, ApJS, 199, 17
Sumiyoshi, K., Yamada, S., Suzuki, H., et al. 2005, ApJ, 629, 922
Suwa, Y., Kotake, K., Takiwaki, T., et al. 2010, PASJ, 62, L49
Suwa, Y., Kotake, K., Takiwaki, T., Liebendörfer, M., & Sato, K. 2011, ApJ, 738, 165
Suwa, Y., Takiwaki, T., Kotake, K., et al. 2013, ApJ, 764, 99
Suzuki, T. K., Sumiyoshi, K., & Yamada, S. 2008, ApJ, 678, 1200
Takahara, M., & Sato, K. 1988, PThPh, 80, 861
Takiwaki, T., & Kotake, K. 2011, ApJ, 743, 30
Takiwaki, T., Kotake, K., Nagataki, S., & Sato, K. 2004, ApJ, 616, 1086
Takiwaki, T., Kotake, K., & Sato, K. 2009, ApJ, 691, 1360
Takiwaki, T., Kotake, K., & Suwa, Y. 2012, ApJ, 749, 98
Takiwaki, T., Kotake, K., & Suwa, Y. 2013, arXiv:1308.5755
Tanaka, M., Kawabata, K. S., Hattori, T., et al. 2012, ApJ, 754, 63
Thompson, T. A., Burrows, A., & Pinto, P. A. 2003, ApJ, 592, 434
Thompson, T. A., Quataert, E., & Burrows, A. 2005, ApJ, 620, 861
Ugliano, M., Janka, H.-T., Marek, A., & Arcones, A. 2012, ApJ, 757, 69
Rampp, M., & Janka, H.-T. 2002, A&A, 396, 361
Rampp, M., & Janka, H.-Th. 2000, ApJL, 539, L33
Rauscher, T., & Thielemann, F.-K. 2000, ADNDT, 75, 1
Wang, L., & Wheeler, J. C. 2008, ARA&A, 46, 433
Wilson, J. R. 1985, in Numerical Astrophysics, ed. J. M. Centrella, J. M. LeBlanc, & R. L. Bowers (Boston: Jones & Bartlett), 422
Wongwathanarat, A., Janka, H.-T., & Müller, E. 2010, ApJL, 725, L106
Woosley, S. E., Heger, A., & Weaver, T. A. 2002, RvMP, 74, 1015
Woosley, S. E., & Weaver, T. A. 1995, ApJS, 101, 181